

This is a pre print version of the following article:

Sound velocities and single-crystal elasticity of hydrous Fo90 olivine to 12 GPa / Faccincani, Luca; Criniti, Giacomo; Kurnosov, Alexander; Ballaran, Tiziana Boffa; Withers, Anthony C.; Mazzucchelli, Maurizio; Nestola, Fabrizio; Coltorti, Massimo. - In: PHYSICS OF THE EARTH AND PLANETARY INTERIORS. - ISSN 0031-9201. - 337:(2023), pp. 1-13. [10.1016/j.pepi.2023.107011]

Terms of use:

The terms and conditions for the reuse of this version of the manuscript are specified in the publishing policy. For all terms of use and more information see the publisher's website.

02/05/2026 22:36

(Article begins on next page)

1 **Sound velocities and single-crystal elasticity of hydrous Fo90 olivine to 12 GPa**

2 Luca Faccincani ^{1,*}, Giacomo Criniti ², Alexander Kurnosov ², Tiziana Boffa Ballaran ², Anthony C.
3 Withers ², Maurizio Mazzucchelli ³, Fabrizio Nestola ⁴ and Massimo Coltorti ^{1,5}

4
5 ¹ *Department of Physics and Earth Sciences, University of Ferrara, Via Saragat 1, 44121 Ferrara,*
6 *Italy*

7 ² *Bayerisches Geoinstitut, University of Bayreuth, Universitätsstraße 30, 95440 Bayreuth, Germany*

8 ³ *Department of Chemical and Geological Sciences, University of Modena and Reggio Emilia, Via*
9 *Campi 103, 41125 Modena, Italy*

10 ⁴ *Department of Geosciences, University of Padua, Via Gradenigo 6, 35131 Padua, Italy*

11 ⁵ *Istituto Nazionale di Geofisica e Vulcanologia (INGV) Sezione di Palermo, Via Ugo la Malfa 153,*
12 *90146 Palermo, Italy*

13
14 * **Corresponding author:** Luca Faccincani; email: luca.faccincani@unife.it

15 **Abstract**

16 Nominally anhydrous minerals (NAMs) may contain significant amounts of water and constitute
17 an important reservoir for mantle hydrogen. The colloquial term ‘water’ in NAMs is related to the
18 presence of hydroxyl-bearing (OH⁻) point defects in their crystal structure, where hydrogen is bonded
19 to lattice oxygen and is charge-balanced by cation vacancies. This hydrous component may therefore
20 have substantial effects on the thermoelastic parameters of NAMs, comparable to other major crystal-
21 chemical substitutions (e.g., Fe, Al). Assessment of water concentrations in natural minerals from
22 mantle xenoliths indicates that olivine commonly stores ~10⁰ – 10² ppm of water. However, the lack
23 of samples originating from depths exceeding ~250 km coupled with the rapid diffusion of hydrogen
24 in olivine at magmatic temperatures makes the determination of the olivine water content in the upper
25 mantle challenging. On the other hand, numerous experimental data show that, at pressures and

26 temperatures corresponding to deep upper mantle conditions, the water storage capacity of olivine
27 increases to 0.2 – 0.5 wt.% H₂O. Therefore, determining the elastic properties of olivine samples with
28 more realistic water contents for deep upper mantle conditions may help in interpreting both seismic
29 velocity anomalies in potentially hydrous regions of Earth's mantle as well as the observed seismic
30 velocity and density contrasts across the 410-km discontinuity.

31 Here, we report simultaneous single-crystal X-ray diffraction and Brillouin scattering experiments
32 at room temperature up to 11.96(2) GPa on hydrous (0.20(3) wt.% H₂O) Fo90 olivine to assess its
33 full elastic tensor. To place further constraints on the effect of hydration on olivine elastic properties,
34 we modelled higher water concentrations in olivine, namely 0.5 wt.% H₂O, using our new accurate
35 data. Although the elastic moduli and pressure derivatives of hydrous Fo90 olivine are slightly
36 different compared to those of the corresponding anhydrous phase, our results demonstrate that the
37 sound wave velocities of hydrous and anhydrous olivines are indistinguishable within uncertainties
38 at pressures corresponding to the base of the upper mantle. Contrary to previous claims, our data
39 suggest that water in olivine is not seismically detectable, at least for contents consistent with deep
40 upper mantle conditions. In addition to that, our data reveal that the hydration of olivine is unlikely
41 to be a key factor in reconciling seismic velocity and density contrasts across the 410-km
42 discontinuity with a pyrolitic mantle.

43

44 **Keywords:** hydrous olivine, Brillouin scattering, elasticity, high pressure; NAMs

45 **1. Introduction**

46 Although commonly referred to as nominally anhydrous minerals (NAMs), the dominant phases
47 of Earth's upper mantle may contain significant amounts of water (e.g., Bell and Rossman, 1992).
48 The occurrence of water in NAMs is closely related to the presence of hydrogen in their crystal
49 structures, which is bonded to oxygen atoms forming hydroxyl-bearing (OH⁻) point defects and its
50 incorporation is typically charge-balanced by the formation of cation vacancies. Olivine, α -
51 (Mg,Fe)₂SiO₄, is considered to be the most abundant mineral of Earth's upper mantle and to constitute

52 about 60 vol.% of pyrolitic phase assemblages (Ringwood, 1975). The water concentration detected
53 in natural olivine samples from mantle xenoliths is generally low, in the order of $10^0 - 10^2$ ppm wt.
54 (Beran and Libowitzky, 2006; Novella et al., 2015; Peslier et al., 2010). Although a growing body of
55 water analyses of olivine is available in the literature (Bonadiman et al., 2009; Peslier, 2010; Xia et
56 al., 2010, and many other reviews), trends between water content and its distribution across different
57 geological settings are still difficult to determine, as well as the actual abundance of water in olivine
58 in the upper mantle. This is due to both the rapid diffusion of hydrogen in olivine at magmatic
59 temperatures (e.g., Demouchy and Mackwell, 2006), which leads to partial dehydration of olivine in
60 mantle xenoliths during their ascent, and the lack of xenoliths originating from depths greater than
61 ~250 km. Even though the fast ascent of kimberlite magmas should prevent dehydration in olivine
62 during xenolith transport (Demouchy et al., 2006; Peslier et al., 2008), in contrast to olivines from
63 xenoliths found in alkali basalts which are commonly affected by H loss (e.g., Peslier et al., 2008),
64 our understanding of how the water content of olivines changes as a function of depth largely relies
65 on experimental studies. Indeed, a plethora of experimental data on water solubility in olivines at
66 pressures and temperatures relevant to the upper mantle are available and indicate much higher water
67 contents compared to those detected in natural olivine samples, especially at deep upper mantle
68 conditions where the water storage capacity of olivine increases to 0.2 – 0.5 wt.% H₂O (e.g., Férot
69 and Bolfan-Casanova, 2012; Hirschmann et al., 2005; Mosenfelder, 2006). Therefore, synthetic
70 olivine samples with a more realistic water content expected for deep upper mantle conditions warrant
71 investigation, as this may improve our understanding of various geodynamic processes operating on
72 Earth (Regenauer-Lieb, 2006, and references therein).

73 Water incorporation in olivine, even in trace amounts, has long been known to have substantial
74 effects on its physical and chemical properties, such as atomic diffusivity, electrical conductivity,
75 thermal conductivity, rheology, and melting (e.g., Chang et al., 2017; Costa and Chakraborty, 2008;
76 Inoue, 1994; Jung and Karato, 2001; Smyth et al., 2006). From a crystal-chemical perspective,
77 hydrogen incorporation in the crystal structure of olivine may occur both in the octahedral M sites,

78 $\text{Mg}^{2+} \leftrightarrow 2\text{H}^+$, and in tetrahedral T sites, $\text{Si}^{4+} \leftrightarrow 4\text{H}^+$ (e.g., Brodholt and Refson, 2000; Hushur et al.,
79 2009; Smyth et al., 2006). Previous experimental studies about the substitution mechanism of water
80 in olivine showed contrasting results, although it was recognized that the synthesis conditions
81 (pressure and SiO_2 activity) were influencing factors (e.g., Bali et al., 2008; Férot and Bolfan-
82 Casanova, 2012; Matveev et al., 2001; Withers and Hirschmann, 2008). However, recent electron
83 microprobe (EPMA) data coupled with transmission Fourier transform infrared spectroscopy (FTIR)
84 analyses (Fei and Katsura, 2020), solid-state nuclear magnetic resonance (NMR) spectroscopy (Xue
85 et al., 2017), and first-principles calculations studies (Umemoto et al., 2011; Xue et al., 2017) suggest
86 that hydrogen substitution in olivine mainly occurs at the T sites at high pressure. Therefore, hydrogen
87 incorporation in the M sites can be ruled out from being the predominant substitution mechanism in
88 olivine under typical mantle conditions, as its occurrence is restricted to shallow depths (≤ 2.5 GPa)
89 and high SiO_2 activity (Bali et al., 2008; Fei and Katsura, 2020; Withers et al., 2011).

90 Despite its possible geophysical relevance, the effect of water on the elastic properties of olivine
91 has been poorly constrained. The only elasticity measurements available in the literature were
92 conducted by Mao et al. (2010) on hydrous (0.9 wt.% H_2O) end-member forsterite (Fo100) single
93 crystals up to 14 GPa and by Jacobsen et al. (2008, 2009) on hydrous (0.8 wt.% H_2O) Fo97 olivine
94 single crystals at ambient pressure. These works showed that the incorporation of water into pure
95 forsterite and near end-member compositions is accompanied by a considerable reduction of the bulk
96 (K_S) and shear (G) moduli at ambient conditions. However, owing to the much larger moduli pressure
97 derivatives of the hydrated samples, K_S and G of the hydrous Fo100 at high pressure are greater than
98 those of the corresponding anhydrous phase (Mao et al., 2010). Nonetheless, the effect of hydration
99 on the elasticity of the more relevant Fo90 olivine mantle composition remains largely unconstrained
100 because no experimental data are available. Furthermore, previous works studied hydrous samples
101 containing 0.8-0.9 wt.% H_2O , which is well above the expected water content for olivine at deep
102 upper mantle conditions (e.g., Férot and Bolfan-Casanova, 2012; Hirschmann et al., 2005;
103 Mosenfelder, 2006).

104 In this work, we set out to investigate the effect of hydration on the elastic properties and sound
105 wave velocities of hydrous Fo90 olivine samples with more realistic water content for deep upper
106 mantle conditions, as it may help in interpreting both seismic velocity anomalies in potentially
107 hydrous regions of Earth's mantle as well as the observed seismic velocity and density contrasts across
108 the 410-km discontinuity. To this aim, we performed simultaneous single-crystal X-ray diffraction
109 (SCXRD) and Brillouin scattering measurements at room temperature up to 11.96(2) GPa on hydrous
110 (0.20(3) wt.% H₂O) Fo90 olivine to constrain its full elastic tensor. By comparing our new accurate
111 data with those available from literature for anhydrous Fo90 olivine, we evaluated the combined
112 effect of H₂O and Fe incorporation on the pressure-dependent elasticity of olivine. Our measurements
113 are suitable to determine the sound wave velocities of hydrous Fo90 olivine at pressures
114 corresponding to the base of the upper mantle, to be integrated in theoretical/experimental studies
115 attempting to constrain the olivine abundance and water content at the 410-km discontinuity.

116 **2. Materials and Methods**

117 Large (200 – 500 μm) and homogeneous single crystals of hydrous Fo90 olivine used in this study
118 were previously synthesized and characterized by Withers et al. (2011, 2012, sample M475). Major
119 element concentrations determined by wavelength-dispersive EPMA analysis indicate the Mg# of
120 synthesized olivines to be 90.2(1), whereas their water content was determined to be ~0.20(3) wt.%
121 based on elastic recoil detection analysis (ERDA) (Withers et al., 2012). Polarized FTIR spectroscopy
122 and secondary ion mass spectroscopy (SIMS) measurements were also conducted on the same
123 sample, showing excellent agreement with one another (Withers et al., 2012).

124 High-pressure Brillouin scattering measurements in DAC are conducted in the so-called platelet
125 geometry (Whitfield et al., 1976). For olivine, at least two crystal platelets with different
126 crystallographic orientations are required to obtain the nine independent elastic stiffness coefficients
127 (c_{ij}) given its orthorhombic symmetry. The full elastic tensor is obtained by a least-square fit of
128 experimentally determined densities and sound wave velocities measured in different crystallographic
129 directions using the Christoffel's equation:

130
$$|c_{ijkl}q_jq_l - \rho v_i^2 \delta_{ik}| = 0 \quad (1)$$

131 where c_{ijkl} are the elastic stiffness coefficients in tensorial notation (e.g., Nye, 1985), q_j and q_l are
132 direction cosines, ρ is the density, v_i are the sound wave velocities and δ_{ik} is the Kronecker delta. To
133 obtain accurate and precise c_{ij} values, it is important that their correlation in the fit procedure is low.
134 This is achieved by using two appropriate crystallographic orientations (Criniti et al., 2021). We used
135 published c_{ij} data for Fo90 olivine (Abramson et al., 1997) to simulate the shear (v_S) and
136 compressional velocities (v_P) for different crystallographic planes. Synthetic v_S and v_P were randomly
137 scattered by up to ± 30 or ± 60 m/s, respectively, to simulate realistic datasets and to obtain realistic
138 uncertainties in the inversion procedure. Platelets with direction cosines (0.32, 0.91, 0.26) and (0.78,
139 0.02, 0.62), corresponding to 101 and 161 *hkl* indices, were chosen for high-pressure measurements.

140 Hydrous Fo90 olivine single crystals were first observed under a polarising microscope and
141 selected based on the absence of inclusions and their sharp optical extinction. Preliminary X-ray
142 diffraction measurements were carried out on a Huber single-crystal diffractometer equipped with a
143 point detector and $MoK\alpha$ radiation, and driven by the software SINGLE (Angel and Finger, 2011).
144 Sharp diffraction peaks (full width half maxima $< 0.055^\circ$) were observed upon omega-scan rotations
145 for each crystal, confirming that they are of high quality. Two crystals were selected and subsequently
146 oriented parallel to the (101) or (161) crystallographic plane, glued on a glass slide and polished on
147 both sides to obtain platelets (crystals X1 and X2, respectively) with a thickness of $\sim 15 \mu\text{m}$. The two
148 platelets were then cut into semi-circular or rectangular shapes (Figure 1) using a FEI Scios focused
149 ion beam (Schulze et al., 2017), operated at 30 nA and 30 kV.

150 High-pressure SCXRD and Brillouin scattering measurements were carried out in a BX-90 piston-
151 cylinder-type diamond anvil cell (DAC) (Kantor et al., 2012) equipped with Almax-Boehler diamond
152 anvils having culets of $500 \mu\text{m}$ in diameter and conical seats with large opening angles (Boehler and
153 De Hantsetters, 2004). A Re gasket was indented to a thickness of $\sim 70 \mu\text{m}$ and drilled with an infrared
154 laser to obtain the sample chamber. The two FIB-cut crystal platelets were loaded into the same
155 sample chamber together with a ruby sphere (Figure 1) for pressure determination following the

156 calibration reported by Shen et al. (2020). Pre-compressed helium was loaded as quasi-hydrostatic
157 pressure transmitting medium using the gas loading apparatus installed at the Bayerisches Geoinstitut,
158 University of Bayreuth (Kurnosov et al., 2008).

159 High-pressure SCXRD and Brillouin scattering measurements were conducted using the system
160 installed at the Bayerisches Geoinstitut, University of Bayreuth (Trots et al., 2011, 2013). The
161 Brillouin scattering system consists of a Coherent Verdi V2 solid-state Nd:YVO₄ laser with a 532 nm
162 single wavelength output and a six-pass Sandercock-type tandem Fabry-Perot interferometer
163 (Sandercock, 1982) equipped with a Hamamatsu C11202-50 detector. A source laser power of 100
164 or 150 mW was used for room pressure and high-pressure measurements, respectively. All
165 measurements were performed in platelet geometry with an external scattering angle of 80°, which
166 was periodically calibrated using a fused silica glass standard. Dispersion curves of sound wave
167 velocities versus crystallographic orientation were collected by rotation of the χ circle of the
168 diffractometer between -170° and 180° at steps of 10° or 20°. Densities were derived at each pressure
169 from single-crystal diffraction measurements, which were performed on the same goniometer using
170 a Huber Eulerian single-crystal X-ray diffractometer equipped with a point detector. The system is
171 coupled with an ultra-high intensity rotating anode X-ray source (MoK α , FR-E⁺ SuperBright from
172 Rigaku) operated at 55 kV and 45 mA and multilayer VaryMaxTM focusing optics, and was driven by
173 the software SINGLE (Angel and Finger, 2011). At each pressure point, 14-18 Bragg reflections for
174 each crystal were centred using the eight position centring method (King and Finger, 1979), and cell
175 parameters were determined by vector least-square refinement (Ralph and Finger, 1982).

176 **3. Results and discussion**

177 **3.1 Compressibility of hydrous Fo90 olivine**

178 High-pressure SCXRD measurements were conducted at seven pressure points, ranging from
179 ambient pressure to ~12 GPa. Unit-cell lattice parameters and volumes of both hydrous Fo90 olivine
180 single crystals investigated in this study are reported in Table 1. The two crystals have slightly
181 different volumes, $V(X1) > V(X2)$, with crystal X1 showing larger uncertainties on the measured

182 lattice parameters. This is due to its crystallographic orientation, which limits the observations in both
183 a^* and c^* . Therefore, lattice parameters measured for crystal X2 are most probably more accurate.
184 The variation with pressure of the lattice parameters and volumes, normalized with respect to their
185 room pressure values, are reported in Figure 2 and compared with literature data. Hydrous olivine is
186 most compressible along the **b**-direction ([010]) and least compressible along the **a**-direction ([100]),
187 with the axial compressibility scheme being $\beta_b > \beta_c > \beta_a$. The same axial compressibility scheme has
188 been also observed for end-member Fo100 (e.g., Downs et al., 1996; Pamato et al., 2019). A third-
189 order Birch-Murnaghan Equation of State (BM3 EoS) has been used to fit the P - V data of both crystals
190 using the EoSFit7c program (Angel et al., 2014). The resulting EoS parameters are: $V_0 = 291.65(2)$
191 \AA^3 , $K_{T0} = 124.5(1.0)$ GPa and $K' = 4.5(2)$. The fitted V_0 value is in excellent agreement (within 1σ)
192 with the unit-cell volume measured at room pressure for crystal X2. Linearized BM3 EoSs have been
193 used to fit the variation with pressure of the a-, b- and c-axis and the resulting EoS parameters are: a_0
194 $= 4.7610(1)$ \AA , $M_{0a} = 539.1(5.7)$ GPa, $M_a' = 23.7(1.4)$, $b_0 = 10.2238(3)$ \AA , $M_{0b} = 283.4(2.8)$ GPa, $M_b' =$
195 $10.7(6)$ and $c_0 = 5.9921(1)$ \AA , $M_{0c} = 372.1(2.6)$ GPa, $M_c' = 12.1(5)$. The axial modulus for the a-axis
196 is much larger than that obtained for the b-axis, similarly to what is observed for the corresponding
197 anhydrous phase Fo90 olivine, as discussed later.

198 Angel et al. (2018) recently reviewed all the published single-crystal data that constrain the elastic
199 properties and EoS of mantle-composition olivine (Fo90 to Fo92), also testing the mutual consistency
200 of the different datasets used. Therefore, data selected by Angel et al. (2018) will be used as a
201 comparison for hydrous olivine. The unit-cell lattice parameters reported by Nestola et al. (2011) and
202 Zha et al. (1998), normalized to their corresponding room pressure values, are compared to the single
203 crystal hydrous Fo90 olivine data obtained in this study (Figure 2). When compared to the P - V and
204 linearized BM3 EoS fits of the hydrous Fo90 olivine data obtained in this study, the relative
205 compression curves (lattice parameters and volumes) for the corresponding anhydrous phase show
206 good agreement. Hence, we do not observe anomalies in the axial compressibility scheme or the unit-
207 cell volume compression of the hydrous phase.

208

209 **3.2 Sound wave velocities of hydrous Fo90 olivine and c_{ij} inversion strategy**

210 Sound wave velocities of hydrous Fo90 olivine were measured at seven pressure points, ranging
211 from ambient pressure to ~12 GPa, i.e., the same conditions of SCXRD measurements (Table 2).
212 Typical Brillouin spectra collected in the low- and high-pressure range (Figure 3a) show distinct and
213 resolved compressional v_P and shear (v_{S1} and v_{S2}) wave velocities peaks for most ranges of rotation
214 angle (χ) (Figure 3b). To obtain the nine elastic stiffness coefficients c_{ij} , the Christoffel's equation
215 (Equation 1) is usually solved using a non-linear least-squares inversion of the density and all the
216 acoustic velocities, collected with varying azimuthal angles, of the crystal platelets at each individual
217 pressure point. This procedure is referred to as individual fit. Individual fits were performed at each
218 pressure point by inverting all the measured acoustic velocities and density data, which were
219 calculated self-consistently from the measured unit-cell volumes. Individual fits converged with small
220 residuals at each pressure point (Figure 3b) thanks to compressional and shear wave velocities being
221 observed for most ranges of rotation angle (χ) and the low correlation between individual elastic
222 stiffness coefficients resulting from the choice of the orientations of the two crystal platelets X1 and
223 X2 used. Uncertainties in the determined c_{ij} values are generally less than 1%, except for c_{12} (< 2%)
224 (Table 2).

225 Recently, a non-conventional fitting procedure for Brillouin data (referred to as global fit) was
226 proposed by Kurnosov et al. (2017) and described in detail in Buchen (2018). It consists of a global
227 inversion of all sound velocity and density data, instead of independently inverting the data measured
228 at each individual pressure point. This is practically done by fitting all sound velocity and density
229 data with third-order finite strain EoSs describing the evolution with pressure of each c_{ij} , using the
230 formalism of Stixrude and Lithgow-Bertelloni (2005):

$$231 \quad c_{ijkl} = (1 + 2f)^{\frac{5}{2}} \{ c_{ijkl,0} + (3K_0 c'_{ijkl,0} - 5c_{ijkl,0})f + \left(6K_0 c'_{ijkl,0} - 14c_{ijkl,0} - \frac{3}{2}K_0 \delta_{kl}^{ij} (3K'_0 - 16) \right) f^2 \} \quad (2)$$

232 where c_{ijkl} is the elastic stiffness coefficient in tensorial notation at a given density (i.e., pressure), f
233 is the finite Eulerian strain defined as $\frac{1}{2} \left[\left(\frac{\rho_0}{\rho} \right)^{\frac{2}{3}} - 1 \right]$, $c_{ijkl,0}$ is the elastic stiffness coefficient at ambient
234 conditions and $c'_{ijkl,0}$ its pressure derivative, K_0 is the bulk modulus at ambient conditions and K'_0 its
235 pressure derivative, and δ^{ijkl} is equal to -3 for c_{1111} , c_{2222} , and c_{3333} and to -1 for the other six
236 independent components of the elastic tensor. Thus, by refining the ambient-pressure stiffness
237 coefficients ($c_{ij,0}$) and their pressure derivatives ($c'_{ij,0}$), a fit of all measured velocities at all pressure
238 points is obtained. This approach has the advantage that all velocity data from all pressure points are
239 used to constrain the c_{ij} s, minimizing the effect of data scattering on the calculated c_{ij} s and thus
240 reducing their estimated uncertainties (Buchen, 2018). Even though this fitting procedure is
241 particularly suited for very high pressure data, where some of the c_{ij} s are poorly constrained due to
242 the lack of observations (e.g., Criniti et al., 2021), it can be applied to any high-pressure sound
243 velocity dataset and the two procedures should yield consistent results as long as the collected data
244 are of high quality, the high-pressure evolution of all c_{ij} is well described by a third-order finite strain
245 EoS, and no phase transition takes place in the investigated pressure interval. Therefore, we also
246 applied the global fit procedure to our dataset, which yielded very consistent results compared to
247 those obtained by individual fits. The c_{ij} s calculated from two procedures show virtually no
248 discrepancies, with values typically identical within two standard deviations (Table 2, Figure 4).

249 Because density is measured at each pressure point, it is possible to calculate pressure without
250 relying on a secondary scale (e.g., ruby) using the relative change in volume of the sample, obtained
251 by X-ray diffraction, and the 3rd-order finite strain equations described above. From these, an
252 expression for the isothermal bulk modulus in the Reuss bound (K_{TR}) as a function of volume is
253 obtained and the absolute pressure (P_{abs}) can be calculated by integrating K_{TR}/V over a given volume
254 interval:

$$255 \quad P_{abs} = \int_{V_0}^V \frac{K_{TR}(V)}{V} dV = 3K_{TR0}f(1+2f)^{\frac{5}{2}} \left[1 + \frac{3}{2}(K'_{TR0} - 4)f \right] \quad (3)$$

256 where $K_{\text{TR}0}$ is the bulk modulus at ambient conditions, $K'_{\text{TR}0}$ is its pressure derivative, f is the finite
 257 Eulerian strain defined as $\frac{1}{2} \left[\left(\frac{V}{V_0} \right)^{\frac{2}{3}} - 1 \right]$. The experimentally determined adiabatic bulk modulus K_{SR}
 258 (Table 2) was converted into K_{TR} using the relations $K_{\text{SR}} = K_{\text{TR}}(1 + \alpha\gamma T)$ and $\alpha = \gamma C_V / K_{\text{TR}} V$. The
 259 thermoelastic parameters used for the conversion are $\theta_D = 644$ K, $\gamma_0 = 1.044$ and $q = 1.88$,
 260 corresponding to Fo90 (Angel et al., 2018), and are here assumed to be H₂O-independent. Then, $K_{\text{TR}0}$
 261 and $K'_{\text{TR}0}$ were calculated by fitting a BM3 EoS to our $K_{\text{T}}-V$ dataset. A comparison between the
 262 absolute pressure and the pressures determined from the ruby fluorescence shift is plotted in
 263 Supplementary Fig. S1, along with the BM3 EoS fits to the $K_{\text{SR}}-\rho$ datasets obtained from the global
 264 and individual fits, which show excellent agreement.

265 Figure 4 shows individual c_{ij} as a function of absolute pressure, as well as selected literature data
 266 for anhydrous Fo90 olivines for comparison, following the re-analysis of all the published single
 267 crystal data proposed by Angel et al. (2018) (Supplementary Table S2). The longitudinal moduli (c_{11} ,
 268 c_{22} and c_{33}), the off-diagonal moduli (c_{12} , c_{13} and c_{33}) and the shear moduli c_{44} and c_{66} follow a nearly
 269 linear increase with pressure, whereas the shear modulus c_{55} exhibits a slightly downward trend
 270 towards higher pressures. The longitudinal moduli c_{11} , c_{22} , c_{33} and the shear moduli c_{44} , c_{55} , c_{66} follow
 271 similar trends with pressure compared to the anhydrous phase; only c_{55} and c_{66} are slightly offset to
 272 lower values in the range of 5 to 10 GPa (Figure 4e). The off-diagonal moduli c_{12} , c_{13} , c_{23} are
 273 characterized by very similar values along the whole pressure interval, with the stiffness scheme being
 274 $c_{23} > c_{12} > c_{13}$. Due to the small differences in the magnitude of the off-diagonal moduli, their values
 275 are frequently the same within uncertainties, especially at high pressure. The off-diagonal moduli c_{12} ,
 276 c_{13} , c_{23} of the anhydrous phase are scattered but show comparable trends with those of the hydrous
 277 phase, especially c_{23} . Even if c_{13} is generally stiffer than c_{12} , in contrast with the hydrous phase, their
 278 systematics is more complex, as either they frequently cross over or are the same within uncertainties.

279 280 **3.3 Elastic Properties of Hydrous Fo90 vs Anhydrous Fo90 Olivine**

281 The adiabatic K_S and G were calculated from the c_{ij} values in the Reuss and Voigt bounds and in
 282 the Voigt-Reuss-Hill average at each experimental pressure point and are reported in Table 2. The
 283 elastic moduli obtained in this study were then fitted with third-order finite strain EoS to obtain the
 284 elastic moduli at ambient conditions (K_{S0} and G_0) and their pressure derivatives (K'_{S0} and G'_0) using
 285 the finite strain EoS of Stixrude and Lithgow-Bertelloni (2005):

$$286 \quad K = (1 + 2f)^{\frac{5}{2}} \left[K_0 + (3K_0K'_0 - 5K_0)f + \frac{27}{2} (K_0K'_0 - 4K_0)f^2 \right] \quad (4)$$

$$287 \quad G = (1 + 2f)^{\frac{5}{2}} \left[G_0 + (3K_0G'_0 - 5G_0)f + \left(6K_0G'_0 - 24K_0 - 14G_0 + \frac{9}{2}K_0K'_0 \right) f^2 \right] \quad (5)$$

288 The EoS parameters for K and G in the Voigt and Reuss bound are reported in Table 4. Both K_S and
 289 G show a monotonic increase with pressure (Figure 5a) and are perfectly described by third-order
 290 EoS.

291 To quantify the effect of 0.20 wt.% H₂O on the Fo90 elastic properties, the EoS parameters for
 292 hydrous Fo90 olivine determined in this study have to be compared to those of the corresponding
 293 anhydrous phase. The elastic behaviour of anhydrous Fo90 olivine has been largely investigated in
 294 the past decades and its full elastic tensor has been constrained by a variety of techniques. Angel et
 295 al. (2018) presented a re-analysis of all available single crystal data for mantle-composition olivine
 296 (Fo90-92) providing best-fit EoS parameters, which were recently used to calculate olivine density
 297 profiles over the upper mantle under different thermal regimes (Faccincani et al., 2021). However, a
 298 comparison of the EoS parameters determined in this study with those from Angel et al. (2018) cannot
 299 be made for two main reasons: (i) a best fit of the shear modulus data is missing, (ii) the fit includes
 300 high-temperature volume data and high-pressure, high-temperature (HP-HT) elasticity data, which
 301 are not available for hydrous Fo90 olivine. For this reason, we refitted the high-pressure elasticity
 302 data (K_S and G) for anhydrous Fo90 originally used in the fit from Angel et al. (2018) with the same
 303 formalism used for hydrous Fo90 olivine (Equations 4 and 5). The data used correspond to Fo90
 304 olivines, and were selected up to ~14 GPa, i.e., the uppermost limit of olivine stability field. In our
 305 examination, we also made a re-analysis of the available shear modulus data to provide the best fit
 306 for G_0 and G'_0 of anhydrous Fo90 olivine. K_S and G were recalculated from the c_{ij} values reported at

307 high pressure by Abramson et al. (1997) where the data are complete (i.e., four pressure points), the
308 data of Zha et al. (1998) (i.e., four pressure points), the data of Mao et al. (2015) (i.e., seven pressure
309 points) and the data of Zhang and Bass (2016) (i.e., five pressure points) (Figure 5b, Supplementary
310 Table S2). The EoS parameters for K_S and G in the Voigt and Reuss bound are reported in Table 4.

311 The EoS parameters for hydrous and anhydrous Fo90 olivine at ambient conditions are marginally
312 different (Table 4). The incorporation of 0.20 wt.% H₂O into the olivine crystal structure causes a
313 reduction in K_{S0} and G_0 of ~1.2% and ~1.6%, respectively, and an increase in K'_{S0} and G'_0 of ~2.9%
314 and ~4.5%, respectively. Therefore, the elastic moduli of hydrous Fo90 olivine at ambient pressure
315 are relatively softer compared to those of anhydrous Fo90 but are characterized by larger derivatives.
316 Indeed, K and G of hydrous Fo90 increase more rapidly with pressure so that the elastic behaviour of
317 hydrous and anhydrous Fo90 olivine becomes indistinguishable within uncertainties at pressures
318 exceeding ~3-4 GPa. This is consistent with a recent high-pressure single-crystal X-ray diffraction
319 study conducted on a sample of Fo95 olivine with a low water content (~0.15 wt.% H₂O) (Xu et al.,
320 2020), where hydrogen substitution is predominantly associated with the T site. As the effect of water
321 on the elastic moduli and their derivatives in our Fo90 and Fo100 (Mao et al., 2010) may also depend
322 on different H substitution mechanisms in olivine, besides distinct water contents, comparisons
323 among different data should be made carefully. The Fo100 single crystals studied by Mao et al. (2010)
324 were synthesized by Smyth et al. (2006), run SZ0408A, to which the reader is referred for synthesis
325 conditions and FTIR spectrum. For this sample, it was suggested that hydration predominantly
326 occurred through the octahedral substitution $Mg^{2+} \leftrightarrow 2H^+$. On the other hand, a tetrahedral
327 substitution $Si^{4+} \leftrightarrow 4H^+$ has been suggested for our sample (Withers et al., 2011). Note, however, that
328 the FTIR spectra of hydrous Fo100 (Smyth et al., 2006, Figure 2) and hydrous Fo90 (Withers et al.,
329 2011, Figure 2) both show strong absorbance features in the identical high wavenumber region,
330 hinting that the two samples should present the same substitution mechanism. Various pieces of
331 evidence suggest that absorption features in the high wavenumber region (~3.450-3.600 cm⁻¹) are
332 related to OH bonding to T sites (Fei and Katsura, 2020; Umemoto et al., 2011; Xue et al., 2017),

333 therefore we may expect that both the Fo100 and Fo90 sample contain predominantly Si vacancies.
 334 The important observation, however, for the aim of this study is that both samples present the same
 335 type of defects and therefore we can compare the effect of hydration on their elastic properties
 336 directly, upon normalization with respect to H₂O concentration. The effect of water on the elastic
 337 parameters can be then expressed as:

$$338 \quad \Delta_{H_2O}M(\%/wt.\% H_2O) = \frac{M_{hydrated} - M_{dry}}{M_{dry}} \times \frac{1}{X_{H_2O}(wt.\%)} \times 100\% \quad (6)$$

339 where M can be K_{S0} , G_0 (in GPa), K'_{S0} or G'_{S0} (non-dimensional) and X_{H_2O} is the water content of the
 340 hydrous sample in wt.%. The obtained results for both Fo90 and Fo100 are reported in Table 4. $\Delta_{H_2O}M$
 341 values are affected by large uncertainties, especially in the case of Fo90. This mostly arises from the
 342 fitting parameters of anhydrous Fo90, which are less well-constrained because four different datasets
 343 were combined in the EoS fit of the elastic moduli (Table 4). $\Delta_{H_2O}K_{S0}$ and $\Delta_{H_2O}G_{S0}$ for Fo90 and
 344 Fo100 are on the margins of being mutually consistent. As predicted by Jacobsen et al. (2008, 2009),
 345 K_{S0} and G_0 of Fo90 are slightly more reduced by H₂O compared to Fo100. However, $\Delta_{H_2O}K'_{S0}$ and
 346 $\Delta_{H_2O}G'_{S0}$ values are in excellent agreement within mutual uncertainties (Table 4). Therefore, the more
 347 pronounced effect observed by Mao et al. (2010) on hydrous Fo100 elastic properties arises by virtue
 348 of the higher water content, and not from a different effect of water in Fe-free and Fe-bearing samples
 349 as shown in Table 4. This also suggests that hydration is most likely to have a linear effect on the
 350 pressure derivatives of olivines.

351

352 **3.4 Effect of Hydration on Sound Wave Velocities of Fo90 Olivine and its Geophysical** 353 **Implications**

354 Using the new experimental data obtained in this study, we calculated the aggregate sound wave
 355 velocities of hydrous Fo90 olivine with 0.20 wt.% H₂O as a function of pressure. Aggregate sound
 356 wave velocities of anhydrous Fo90 olivine are compared with those for hydrous olivine (Figure 6).
 357 As the effect of temperature on the elasticity of hydrous olivine is currently unknown, all the
 358 calculations were performed at 300 K. The effect of water on the thermal expansion of hydrous (~2.5

359 wt.% H₂O) wadsleyite and ringwoodite, i.e., the high-pressure polymorphs of olivine, seems to be
360 negligible (Inoue et al. 2004). Therefore, in virtue of the comparatively lower water content of our
361 hydrous olivine, H₂O is not expected to have a significant effect on the thermal expansion of olivine.

362 The v_P and v_S of hydrous Fo90 follow similar trends to those of the elastic moduli (Figure 6), with
363 velocities being lower than in anhydrous Fo90 by 0.8% and 0.9%, respectively, at ambient conditions
364 and becoming the same within uncertainty above 5 GPa. Mao et al. (2010) showed that v_P and v_S of
365 the hydrous Fo100 cross and exceed those of the corresponding anhydrous phase at about 4 and 3
366 GPa, respectively, and rapidly diverge at higher pressure. The prominent rise of v_P and v_S with
367 increasing pressure is due to the higher water content of the hydrous Fo100 sample employed by Mao
368 et al. (2010) and not to a different effect of water in Fe-free and Fe-bearing samples, as shown in
369 Table 4.

370 The 410-km global seismic discontinuity is widely accepted to be caused by the phase transition
371 of olivine to its high pressure polymorph wadsleyite (Frost, 2008). Several works attempted to
372 constrain the bulk olivine content in the upper mantle by comparing sound wave velocities of olivine
373 and wadsleyite, calculated from either experimental or computational mineral physics data, with the
374 observed seismic velocity contrasts across the discontinuity (e.g., Bass and Anderson, 1984;
375 Dziewonski and Anderson, 1981; Núñez-Valdez et al., 2013; Wang et al., 2014, 2019). However, the
376 calculated velocity contrasts across the discontinuity for a pyrolite composition (~60 vol.% olivine)
377 are not consistent with global 1-D seismic models (e.g., Preliminary Earth Reference Model, PREM,
378 or AK135; Dziewonski and Anderson, 1981; Kennett et al., 1995), pointing towards a bottom upper
379 mantle that is less olivine-rich than pyrolite. Considering the reduction of the sound wave velocities
380 of wadsleyite due to the incorporation of water (Mao et al., 2008a, 2008b), it was proposed that water
381 dissolved in olivine and wadsleyite may reconcile the pyrolite model with seismological observations.
382 Water is preferentially partitioned in wadsleyite ($D_{\text{wad/ol}} = 6$; Thio et al., 2016) and whether the
383 presence of water can resolve seismological observations with pyrolitic mantle olivine contents will
384 depend on both the expected amount of water in olivine and to what extents it affects v_P and v_S of

385 olivine. Available experimental data for hydrous olivine indicate storage capacities up to 0.9 wt.%
386 (Smyth et al., 2006), but the water content of olivine under relevant deep upper mantle conditions
387 will be much lower, around 0.2 – 0.5 wt.% H₂O (e.g., Férot and Bolfan-Casanova, 2012; Hirschmann
388 et al., 2005; Mosenfelder, 2006). In this regard, our data are particularly significant and indicate that
389 the incorporation of ~0.20 wt.% H₂O into Fo90 olivine crystal structure does not significantly affect
390 its v_P and v_S at high pressure. To explore whether the presence of higher water contents in olivine
391 would cause greater effects on its v_P and v_S , we used equation (6) to calculate the sound velocities of
392 Fo90 hosting 0.5 wt.% H₂O (Table 4, Figures 5c-6c). Because hydration causes an increase in the
393 unit-cell volume, we recalculated the room pressure volume of Fo90 with 0.5 wt.% H₂O using the
394 factor $+5.5 [A^3] \times 10^{-5} \times \text{H}_2\text{O} [\text{ppm}]$ according to the expression from Smyth et al. (2006), and then
395 converted the resulting volume into density. The calculated sound wave velocities for Fo90 with 0.5
396 wt.% H₂O are reported in Figure 6c and compared to those of hydrous Fo90 with 0.20 wt.% H₂O and
397 anhydrous Fo90. Although the incorporation of 0.5 wt.% H₂O into Fo90 olivine strongly reduces its
398 elastic moduli and sound wave velocities at ambient pressure (Table 4, Figures 5c-6c), v_P and v_S of
399 the hydrous phase become indistinguishable within uncertainties with those of the anhydrous phase
400 at pressures exceeding ~9 and ~12 GPa, owing to the larger K'_{S0} and G'_0 . This advises caution when
401 speculating the water content in the deep upper mantle based on its effect on olivine elastic properties
402 and seismic wave velocities. Furthermore, our data also suggest that H₂O incorporation in olivine
403 may not reconcile seismological observations at the 410-km discontinuity with a pyrolitic mantle,
404 although we are aware that direct determinations of sound wave velocities of hydrous olivine and
405 hydrous wadsleyite at combined HP–HT (e.g., Buchen et al., 2018) are needed to refine these
406 findings.

407 The discrepancy between the observed and calculated wave velocities for a pyrolite composition
408 may also arise from strong variations of olivine content and upper mantle lithologies near the 410-
409 km seismic discontinuity, for which corroborating evidence has been found by Zhang and Bass
410 (2016). Indeed, olivine contents inferred from regional seismic models of the Pacific region are

411 extremely variable and increase from approximately 20 – 40 % in the central Pacific to 60 – 90 % in
412 the western U.S. and eastern Pacific regions. Given the indistinguishable seismic behaviour of
413 hydrous and anhydrous Fo90 olivine at high pressure, we argue that this high degree of heterogeneity
414 does not stem from the potentially different responses of dry and wet regions of the deep upper mantle,
415 but rather may arise from actual variations in olivine content.

416 **4. Concluding remarks**

417 The sound velocities and single-crystal elastic coefficients of Fo90 olivine with 0.20 wt.% H₂O
418 were measured up to ~12 GPa at room temperature by simultaneous single-crystal X-ray diffraction
419 and Brillouin scattering experiments. Compared to the anhydrous phase, *K* and *G* of hydrous Fo90 at
420 ambient conditions are slightly offset to lower values, while their pressure derivatives are slightly
421 larger. Nonetheless, the elastic behaviour of hydrous and anhydrous Fo90 olivine becomes
422 indistinguishable within uncertainties at pressures corresponding to the base of the upper mantle.
423 Using our new accurate data, we investigated the effect of hydration on aggregate sound velocities of
424 Fo90. At ambient pressure, the compressional and shear wave velocities of hydrous Fo90 with 0.2 –
425 0.5 wt.% H₂O are slightly slower compared to those of the hydrous phase, but become
426 indistinguishable within uncertainties at deep upper mantle conditions. Therefore, if amounts of water
427 were to be incorporated into Fo90 olivine crystal structure, its elastic and seismic behaviour at high
428 pressure may remain unchanged. Based on our findings, we suggest that water in olivine is not
429 seismically detectable, at least for contents up to 0.2 – 0.5 wt.%, i.e., the amount of water expected
430 in olivine at deep upper mantle conditions. We therefore advise caution about speculations of the
431 water content in the deep upper mantle based on its effect on olivine elastic properties and sound
432 wave velocities. In addition, our data also suggest that the hydration of olivine is unlikely to be a key
433 factor in reconciling seismic velocity and density contrasts across the 410-km discontinuity with a
434 pyrolitic mantle.

435 **Author contribution statement**

436 [L.F.] Conceptualization, Methodology, Formal analysis, Investigation, Data Curation, Writing–
437 Original Draft, Writing–Review & Editing; [G.C.]: Methodology, Formal analysis, Investigation,
438 Data Curation, Writing–Review & Editing; [A.K.]: Methodology, Investigation, Writing–Review &
439 Editing; [T.B.B.]: Methodology, Investigation, Writing–Review & Editing, Supervision; [A.W.]:
440 Investigation, Writing–Review & Editing; [M.M.]: Writing–Review & Editing, Supervision; [F.N.]:
441 Writing–Review & Editing, Supervision; [M.C.]: Conceptualization, Writing–Review & Editing,
442 Supervision.

443 **Declaration of Competing Interest**

444 The authors declare that they have no known competing financial interests or personal
445 relationships that could have appeared to influence the work reported in this paper.

446 **Acknowledgements**

447 The authors would like to thank R. Njul for his help in double–side polishing the two single
448 crystals to platelets and D. Wiesner for her help in the operation of the FIB device. L.F. acknowledges
449 Istituto Nazionale di Geofisica e Vulcanologia (INGV) for funding his Ph.D. project (XXXV cycle)
450 with thematic ‘Links between rheology, mineralogy and composition of the Earth's mantle’ and the
451 University of Ferrara for the 2021 IUSS international mobility program. This research was also
452 supported by the Italian National Research Program (PRIN Grant 20178LPCPW ‘Micro to Macro –
453 How to unravel the nature of the Large Magmatic Events’ to M.C.)

454 **Data Availability**

455 All data derived from this research are presented in the enclosed tables, figures, and
456 supplementary material.

457 **References**

458 Abramson, E.H., Brown, J.M., Slutsky, L.J., Zaug, J., 1997. The elastic constants of San Carlos

459 olivine to 17 GPa. *J. Geophys. Res. Solid Earth* 102, 12253–12263.
460 <https://doi.org/10.1029/97JB00682>

461 Angel, R.J., Alvaro, M., Gonzalez-Platas, J., 2014. EosFit7c and a Fortran module (library) for
462 equation of state calculations. *Zeitschrift für Krist. - Cryst. Mater.* 229, 405–419.
463 <https://doi.org/10.1515/zkri-2013-1711>

464 Angel, R.J., Alvaro, M., Nestola, F., 2018. 40 years of mineral elasticity: a critical review and a
465 new parameterisation of equations of state for mantle olivines and diamond inclusions. *Phys. Chem.
466 Miner.* 45, 95–113. <https://doi.org/10.1007/s00269-017-0900-7>

467 Angel, R.J., Finger, L.W., 2011. SINGLE : a program to control single-crystal diffractometers. *J.
468 Appl. Crystallogr.* 44, 247–251. <https://doi.org/10.1107/S0021889810042305>

469 Bali, E., Bolfan-Casanova, N., Koga, K.T., 2008. Pressure and temperature dependence of H
470 solubility in forsterite: An implication to water activity in the Earth interior. *Earth Planet. Sci. Lett.*
471 268, 354–363. <https://doi.org/10.1016/j.epsl.2008.01.035>

472 Bass, J.D., Anderson, D.L., 1984. Composition of the upper mantle: Geophysical tests of two
473 petrological models. *Geophys. Res. Lett.* 11, 229–232. <https://doi.org/10.1029/GL011i003p00229>

474 Bell, D.R., Rossman, G.R., 1992. Water in Earth's Mantle: The Role of Nominally Anhydrous
475 Minerals. *Science* (80-.). 255, 1391–1397. <https://doi.org/10.1126/science.255.5050.1391>

476 Beran, A., Libowitzky, E., 2006. Water in natural mantle minerals II: Olivine, garnet and
477 accessory minerals, in: *Reviews in Mineralogy and Geochemistry 62: Water in Nominally Anhydrous
478 Minerals*. pp. 169–192. <https://doi.org/10.2138/rmg.2006.62.8>

479 Boehler, R., De Hantsetters, K., 2004. New anvil designs in diamond-cells. *High Press. Res.* 24,
480 391–396. <https://doi.org/10.1080/08957950412331323924>

481 Bonadiman, C., Hao, Y., Coltorti, M., Dallai, L., Faccini, B., Huang, Y.X., 2009. Water contents
482 of pyroxenes in intraplate lithospheric mantle. *Eur. J. Mineral.* 21, 637–647.
483 <https://doi.org/10.1127/0935-1221/2009/0021-1935>

484 Brodholt, J.P., Refson, K., 2000. An ab initio study of hydrogen in forsterite and a possible

485 mechanism for hydrolytic weakening. *J. Geophys. Res. Solid Earth* 105, 18977–18982.
486 <https://doi.org/10.1029/2000JB900057>

487 Buchen, J., 2018. *The Elastic Properties of Wadsleyite and Stishovite at High Pressures: Tracing*
488 *Deep Earth Material Cycles*. University of Bayreuth. https://doi.org/10.15495/EPub_UBT_00004410

489 Buchen, J., Marquardt, H., Speziale, S., Kawazoe, T., Boffa Ballaran, T., Kurnosov, A., 2018.
490 High-pressure single-crystal elasticity of wadsleyite and the seismic signature of water in the shallow
491 transition zone. *Earth Planet. Sci. Lett.* 498, 77–87. <https://doi.org/10.1016/j.epsl.2018.06.027>

492 Chang, Y.-Y., Hsieh, W.-P., Tan, E., Chen, J., 2017. Hydration-reduced lattice thermal
493 conductivity of olivine in Earth's upper mantle. *Proc. Natl. Acad. Sci.* 114, 4078–4081.
494 <https://doi.org/10.1073/pnas.1616216114>

495 Costa, F., Chakraborty, S., 2008. The effect of water on Si and O diffusion rates in olivine and
496 implications for transport properties and processes in the upper mantle. *Phys. Earth Planet. Inter.* 166,
497 11–29. <https://doi.org/10.1016/j.pepi.2007.10.006>

498 Criniti, G., Kurnosov, A., Boffa Ballaran, T., Frost, D.J., 2021. Single-Crystal Elasticity of
499 MgSiO₃ Bridgmanite to Mid-Lower Mantle Pressure. *J. Geophys. Res. Solid Earth* 126.
500 <https://doi.org/10.1029/2020JB020967>

501 Demouchy, S., Jacobsen, S.D., Gaillard, F., Stern, C.R., 2006. Rapid magma ascent recorded by
502 water diffusion profiles in mantle olivine. *Geology* 34, 429. <https://doi.org/10.1130/G22386.1>

503 Demouchy, S., Mackwell, S., 2006. Mechanisms of hydrogen incorporation and diffusion in iron-
504 bearing olivine. *Phys. Chem. Miner.* 33, 347–355. <https://doi.org/10.1007/s00269-006-0081-2>

505 Downs, R.T., Zha, C.-S., Duffy, T.S., Finger, L.W., 1996. The equation of state of forsterite to
506 17.2 GPa and effects of pressure media. *Am. Mineral.* 81, 51–55. [https://doi.org/10.2138/am-1996-](https://doi.org/10.2138/am-1996-1-207)
507 [1-207](https://doi.org/10.2138/am-1996-1-207)

508 Dziewonski, A.M., Anderson, D.L., 1981. Preliminary reference Earth model. *Phys. Earth Planet.*
509 *Inter.* 25, 297–356. [https://doi.org/10.1016/0031-9201\(81\)90046-7](https://doi.org/10.1016/0031-9201(81)90046-7)

510 Faccincani, L., Faccini, B., Casetta, F., Mazzucchelli, M., Nestola, F., Coltorti, M., 2021. EoS of

511 mantle minerals coupled with composition and thermal state of the lithosphere: Inferring the density
512 structure of peridotitic systems. *Lithos* 404–405, 106483.
513 <https://doi.org/10.1016/j.lithos.2021.106483>

514 Fei, H., Katsura, T., 2020. Pressure Dependence of Proton Incorporation and Water Solubility in
515 Olivine. *J. Geophys. Res. Solid Earth* 125, 1–13. <https://doi.org/10.1029/2019JB018813>

516 Férot, A., Bolfan-Casanova, N., 2012. Water storage capacity in olivine and pyroxene to 14GPa:
517 Implications for the water content of the Earth’s upper mantle and nature of seismic discontinuities.
518 *Earth Planet. Sci. Lett.* 349–350, 218–230. <https://doi.org/10.1016/j.epsl.2012.06.022>

519 Frost, D.J., 2008. The Upper Mantle and Transition Zone. *Elements* 4, 171–176.
520 <https://doi.org/10.2113/GSELEMENTS.4.3.171>

521 Hirschmann, M.M., Aubaud, C., Withers, A.C., 2005. Storage capacity of H₂O in nominally
522 anhydrous minerals in the upper mantle. *Earth Planet. Sci. Lett.* 236, 167–181.
523 <https://doi.org/10.1016/j.epsl.2005.04.022>

524 Hushur, A., Manghnani, M.H., Smyth, J.R., Nestola, F., Frost, D.J., 2009. Crystal chemistry of
525 hydrous forsterite and its vibrational properties up to 41 GPa. *Am. Mineral.* 94, 751–760.
526 <https://doi.org/10.2138/am.2009.2990>

527 Inoue, T., 1994. Effect of water on melting phase relations and melt composition in the system
528 Mg₂SiO₄-MgSiO₃-H₂O up to 15 GPa. *Phys. Earth Planet. Inter.* 85, 237–263.
529 [https://doi.org/10.1016/0031-9201\(94\)90116-3](https://doi.org/10.1016/0031-9201(94)90116-3)

530 Inoue, T., Tanimoto, Y., Irifune, T., Suzuki, T., Fukui, H., Ohtaka, O., 2004. Thermal expansion
531 of wadsleyite, ringwoodite, hydrous wadsleyite and hydrous ringwoodite. *Phys. Earth Planet. Inter.*
532 143–144, 279–290. <https://doi.org/10.1016/j.pepi.2003.07.021>

533 Jacobsen, S.D., Jiang, F., Mao, Z., Duffy, T.S., Smyth, J.R., Holl, C.M., Frost, D.J., 2009.
534 Correction to “Effects of hydration on the elastic properties of olivine.” *Geophys. Res. Lett.* 36,
535 L12302. <https://doi.org/10.1029/2009GL038660>

536 Jacobsen, S.D., Jiang, F., Mao, Z., Duffy, T.S., Smyth, J.R., Holl, C.M., Frost, D.J., 2008. Effects

537 of hydration on the elastic properties of olivine. *Geophys. Res. Lett.* 35, L14303.
538 <https://doi.org/10.1029/2008GL034398>

539 Jung, H., Karato, S.-I., 2001. Effects of water on dynamically recrystallized grain-size of olivine.
540 *J. Struct. Geol.* 23, 1337–1344. [https://doi.org/10.1016/S0191-8141\(01\)00005-0](https://doi.org/10.1016/S0191-8141(01)00005-0)

541 Kantor, I., Prakapenka, V., Kantor, A., Dera, P., Kurnosov, A., Sinogeikin, S., Dubrovinskaia, N.,
542 Dubrovinsky, L., 2012. BX90: A new diamond anvil cell design for X-ray diffraction and optical
543 measurements. *Rev. Sci. Instrum.* 83, 125102. <https://doi.org/10.1063/1.4768541>

544 Kennett, B.L.N., Engdahl, E.R., Buland, R., 1995. Constraints on seismic velocities in the Earth
545 from traveltimes. *Geophys. J. Int.* 122, 108–124. [https://doi.org/10.1111/j.1365-](https://doi.org/10.1111/j.1365-246X.1995.tb03540.x)
546 [246X.1995.tb03540.x](https://doi.org/10.1111/j.1365-246X.1995.tb03540.x)

547 King, H.E., Finger, L.W., 1979. Diffracted beam crystal centering and its application to high-
548 pressure crystallography. *J. Appl. Crystallogr.* 12, 374–378.
549 <https://doi.org/10.1107/S0021889879012723>

550 Kurnosov, A., Kantor, I., Boffa-Ballaran, T., Lindhardt, S., Dubrovinsky, L., Kuznetsov, A.,
551 Zehnder, B.H., 2008. A novel gas-loading system for mechanically closing of various types of
552 diamond anvil cells. *Rev. Sci. Instrum.* 79, 045110. <https://doi.org/10.1063/1.2902506>

553 Kurnosov, A., Marquardt, H., Frost, D.J., Ballaran, T.B., Ziberna, L., 2017. Evidence for a Fe³⁺-
554 rich pyrolitic lower mantle from (Al,Fe)-bearing bridgmanite elasticity data. *Nature* 543, 543–546.
555 <https://doi.org/10.1038/nature21390>

556 Mao, Z., Fan, D., Lin, J.-F., Yang, J., Tkachev, S.N., Zhuravlev, K., Prakapenka, V.B., 2015.
557 Elasticity of single-crystal olivine at high pressures and temperatures. *Earth Planet. Sci. Lett.* 426,
558 204–215. <https://doi.org/10.1016/j.epsl.2015.06.045>

559 Mao, Z., Jacobsen, S.D., Jiang, F., Smyth, J.R., Holl, C.M., Duffy, T.S., 2008a. Elasticity of
560 hydrous wadsleyite to 12 GPa: Implications for Earth's transition zone. *Geophys. Res. Lett.* 35,
561 L21305. <https://doi.org/10.1029/2008GL035618>

562 Mao, Z., Jacobsen, S.D., Jiang, F., Smyth, J.R., Holl, C.M., Frost, D.J., Duffy, T.S., 2010.

563 Velocity crossover between hydrous and anhydrous forsterite at high pressures. *Earth Planet. Sci.*
564 *Lett.* 293, 250–258. <https://doi.org/10.1016/j.epsl.2010.02.025>

565 Mao, Z., Jacobsen, S.D., Jiang, F.M., Smyth, J.R., Holl, C.M., Frost, D.J., Duffy, T.S., 2008b.
566 Single-crystal elasticity of wadsleyites, β -Mg₂SiO₄, containing 0.37–1.66 wt.% H₂O. *Earth Planet.*
567 *Sci. Lett.* 268, 540–549. <https://doi.org/10.1016/j.epsl.2008.01.023>

568 Matveev, S., O’neill, H.S.C., Ballhaus, C., Taylor, W.R., Green, D.H., 2001. Effect of Silica
569 Activity on OH- IR Spectra of Olivine: Implications for Low-aSiO₂ Mantle Metasomatism. *J. Petrol.*
570 42, 721–729. <https://doi.org/10.1093/petrology/42.4.721>

571 Mosenfelder, J.L., 2006. Hydrogen incorporation in olivine from 2-12 GPa. *Am. Mineral.* 91,
572 285–294. <https://doi.org/10.2138/am.2006.1943>

573 Nestola, F., Nimis, P., Ziberna, L., Longo, M., Marzoli, A., Harris, J.W., Manghnani, M.H.,
574 Fedortchouk, Y., 2011. First crystal-structure determination of olivine in diamond: Composition and
575 implications for provenance in the Earth’s mantle. *Earth Planet. Sci. Lett.* 305, 249–255.
576 <https://doi.org/10.1016/j.epsl.2011.03.007>

577 Novella, D., Bolfan-Casanova, N., Nestola, F., Harris, J.W., 2015. H₂O in olivine and garnet
578 inclusions still trapped in diamonds from the Siberian craton: Implications for the water content of
579 cratonic lithosphere peridotites. *Lithos* 230, 180–183. <https://doi.org/10.1016/j.lithos.2015.05.013>

580 Núñez-Valdez, M., Wu, Z., Yu, Y.G., Wentzcovitch, R.M., 2013. Thermal elasticity of (Fe_x,Mg
581 1-x) SiO₄ olivine and wadsleyite. *Geophys. Res. Lett.* 40, 290–294.
582 <https://doi.org/10.1002/grl.50131>

583 Nye, J.F., 1985. *Physical properties of crystals: their representation by tensors and matrices.*
584 Oxford university press.

585 Pamato, M.G., Nestola, F., Novella, D., Smyth, J.R., Pasqual, D., Gatta, G.D., Alvaro, M., Secco,
586 L., 2019. The High-Pressure Structural Evolution of Olivine along the Forsterite–Fayalite Join.
587 *Minerals* 9, 790. <https://doi.org/10.3390/min9120790>

588 Peslier, A.H., 2010. A review of water contents of nominally anhydrous natural minerals in the

589 mantles of Earth, Mars and the Moon. *J. Volcanol. Geotherm. Res.* 197, 239–258.
590 <https://doi.org/10.1016/j.jvolgeores.2009.10.006>

591 Peslier, A.H., Woodland, A.B., Bell, D.R., Lazarov, M., 2010. Olivine water contents in the
592 continental lithosphere and the longevity of cratons. *Nature* 467, 78–81.
593 <https://doi.org/10.1038/nature09317>

594 Peslier, A.H., Woodland, A.B., Wolff, J.A., 2008. Fast kimberlite ascent rates estimated from
595 hydrogen diffusion profiles in xenolithic mantle olivines from southern Africa. *Geochim.*
596 *Cosmochim. Acta* 72, 2711–2722. <https://doi.org/10.1016/j.gca.2008.03.019>

597 Ralph, R.L., Finger, L.W., 1982. A computer program for refinement of crystal orientation matrix
598 and lattice constants from diffractometer data with lattice symmetry constraints. *J. Appl. Crystallogr.*
599 15, 537–539. <https://doi.org/10.1107/S0021889882012539>

600 Regenauer-Lieb, K., 2006. Water and Geodynamics. *Rev. Mineral. Geochemistry* 62, 451–473.
601 <https://doi.org/10.2138/rmg.2006.62.19>

602 Ringwood, A.E., 1975. *Composition and Petrology of the Earth's Mantle*, Mac Graw-Hill Book
603 Company.

604 Sandercock, J.R., 1982. Trends in brillouin scattering: Studies of opaque materials, supported
605 films, and central modes, in: Cardona, M., Güntherodt, G. (Eds.), *Light Scattering in Solids III: Recent Results*. Springer Berlin Heidelberg, Berlin, Heidelberg, pp. 173–206.
606 https://doi.org/10.1007/3540115137_6

607

608 Schulze, K., Buchen, J., Marquardt, K., Marquardt, H., 2017. Multi-sample loading technique for
609 comparative physical property measurements in the diamond-anvil cell. *High Press. Res.* 37, 159–
610 169. <https://doi.org/10.1080/08957959.2017.1299719>

611 Shen, G., Wang, Y., Dewaele, A., Wu, C., Fratanduono, D.E., Eggert, J., Klotz, S., Dziubek, K.F.,
612 Loubeyre, P., Fat'yanov, O. V., Asimow, P.D., Mashimo, T., Wentzcovitch, R.M.M., 2020. Toward
613 an international practical pressure scale: A proposal for an IPPS ruby gauge (IPPS-Ruby2020). *High*
614 *Press. Res.* 40, 299–314. <https://doi.org/10.1080/08957959.2020.1791107>

615 Smyth, J.R., Frost, D.J., Nestola, F., Holl, C.M., Bromiley, G., 2006. Olivine hydration in the
616 deep upper mantle: Effects of temperature and silica activity. *Geophys. Res. Lett.* 33, L15301.
617 <https://doi.org/10.1029/2006GL026194>

618 Stixrude, L., Lithgow-Bertelloni, C., 2005. Thermodynamics of mantle minerals - I. Physical
619 properties. *Geophys. J. Int.* 162, 610–632. <https://doi.org/10.1111/j.1365-246X.2005.02642.x>

620 Thio, V., Cobden, L., Trampert, J., 2016. Seismic signature of a hydrous mantle transition zone.
621 *Phys. Earth Planet. Inter.* 250, 46–63. <https://doi.org/10.1016/j.pepi.2015.11.005>

622 Trots, D.M., Kurnosov, A., Ballaran, T.B., Tkachev, S., Zhuravlev, K., Prakapenka, V.,
623 Berkowski, M., Frost, D.J., 2013. The Sm:YAG primary fluorescence pressure scale. *J. Geophys.*
624 *Res. Solid Earth* 118, 5805–5813. <https://doi.org/10.1002/2013JB010519>

625 Trots, D.M., Kurnosov, A., Vasylechko, L., Berkowski, M., Boffa Ballaran, T., Frost, D.J., 2011.
626 Elasticity and equation of state of Li₂B₄O₇. *Phys. Chem. Miner.* 38, 561–567.
627 <https://doi.org/10.1007/s00269-011-0428-1>

628 Umemoto, K., Wentzcovitch, R.M., Hirschmann, M.M., Kohlstedt, D.L., Withers, A.C., 2011. A
629 first-principles investigation of hydrous defects and IR frequencies in forsterite: The case for Si
630 vacancies. *Am. Mineral.* 96, 1475–1479. <https://doi.org/10.2138/am.2011.3720>

631 Wang, J., Bass, J.D., Kastura, T., 2014. Elastic properties of iron-bearing wadsleyite to 17.7GPa:
632 Implications for mantle mineral models. *Phys. Earth Planet. Inter.* 228, 92–96.
633 <https://doi.org/10.1016/j.pepi.2014.01.015>

634 Wang, W., Walter, M.J., Peng, Y., Redfern, S., Wu, Z., 2019. Constraining olivine abundance
635 and water content of the mantle at the 410-km discontinuity from the elasticity of olivine and
636 wadsleyite. *Earth Planet. Sci. Lett.* 519, 1–11. <https://doi.org/10.1016/j.epsl.2019.04.018>

637 Whitfield, C.H., Brody, E.M., Bassett, W.A., 1976. Elastic moduli of NaCl by Brillouin scattering
638 at high pressure in a diamond anvil cell. *Rev. Sci. Instrum.* 47, 942–947.
639 <https://doi.org/10.1063/1.1134778>

640 Withers, A.C., Bureau, H., Raepsaet, C., Hirschmann, M.M., 2012. Calibration of infrared

641 spectroscopy by elastic recoil detection analysis of H in synthetic olivine. *Chem. Geol.* 334, 92–98.
642 <https://doi.org/10.1016/j.chemgeo.2012.10.002>

643 Withers, A.C., Hirschmann, M.M., 2008. Influence of temperature, composition, silica activity
644 and oxygen fugacity on the H₂O storage capacity of olivine at 8 GPa. *Contrib. to Mineral. Petrol.*
645 156, 595–605. <https://doi.org/10.1007/s00410-008-0303-3>

646 Withers, A.C., Hirschmann, M.M., Tenner, T.J., 2011. The effect of Fe on olivine H₂O storage
647 capacity: Consequences for H₂O in the martian mantle. *Am. Mineral.* 96, 1039–1053.
648 <https://doi.org/10.2138/am.2011.3669>

649 Xia, Q.-K., Hao, Y., Li, P., Deloule, E., Coltorti, M., Dallai, L., Yang, X., Feng, M., 2010. Low
650 water content of the Cenozoic lithospheric mantle beneath the eastern part of the North China Craton.
651 *J. Geophys. Res.* 115, B07207. <https://doi.org/10.1029/2009JB006694>

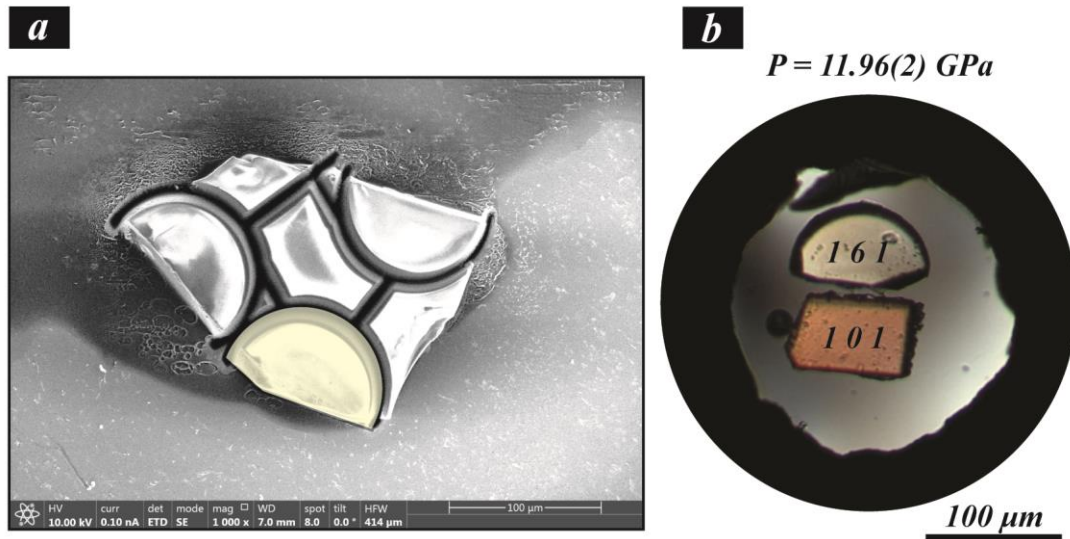
652 Xu, J., Fan, D., Zhang, D., Li, B., Zhou, W., Dera, P.K., 2020. Investigation of the crystal structure
653 of a low water content hydrous olivine to 29.9 GPa: A high-pressure single-crystal X-ray diffraction
654 study. *Am. Mineral.* 105, 1857–1865. <https://doi.org/10.2138/am-2020-7444>

655 Xue, X., Kanzaki, M., Turner, D., Loroch, D., 2017. Hydrogen incorporation mechanisms in
656 forsterite: New insights from ¹H and ²⁹Si NMR spectroscopy and first-principles calculation. *Am.*
657 *Mineral.* 102, 519–536. <https://doi.org/10.2138/am-2017-5878>

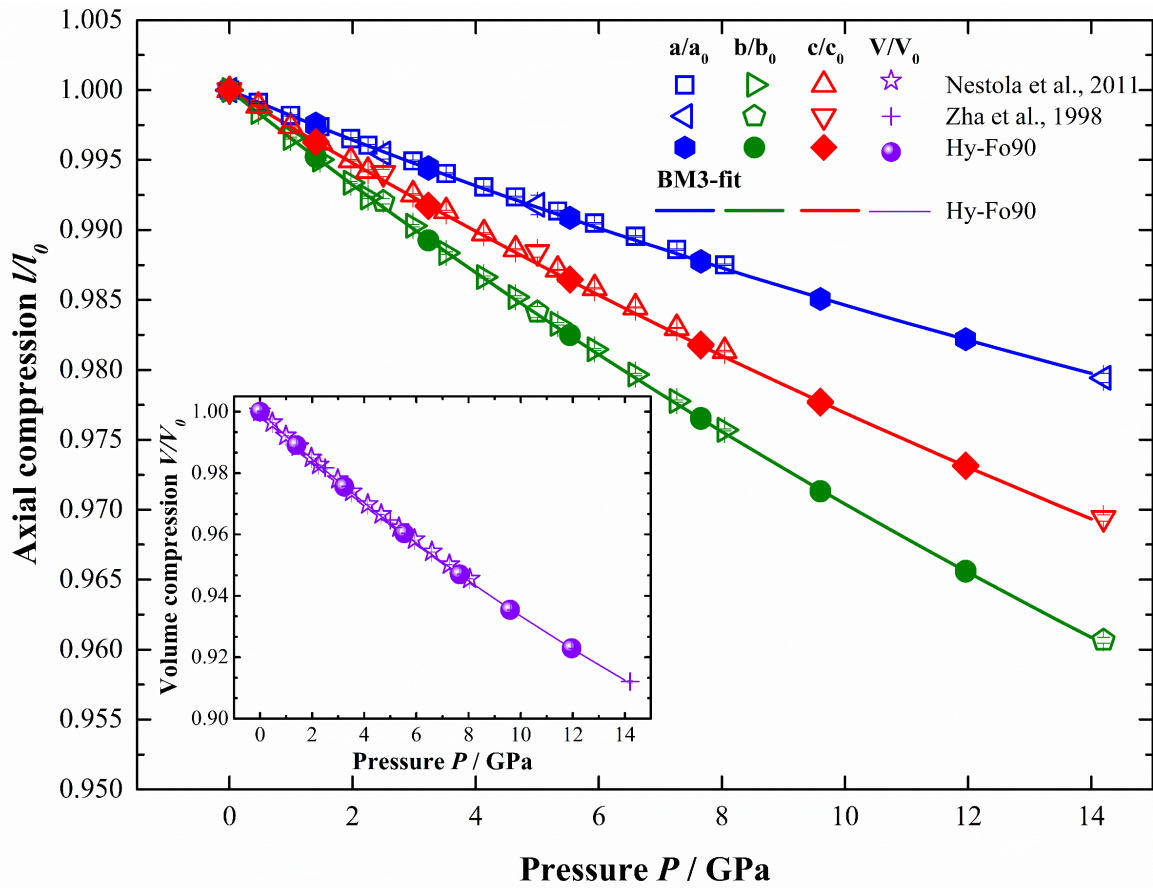
658 Zha, C., Duffy, T.S., Downs, R.T., Mao, H., Hemley, R.J., 1998. Brillouin scattering and X-ray
659 diffraction of San Carlos olivine: direct pressure determination to 32 GPa. *Earth Planet. Sci. Lett.*
660 159, 25–33. [https://doi.org/10.1016/S0012-821X\(98\)00063-6](https://doi.org/10.1016/S0012-821X(98)00063-6)

661 Zhang, J.S., Bass, J.D., 2016. Sound velocities of olivine at high pressures and temperatures
662 and the composition of Earth's upper mantle. *Geophys. Res. Lett.* 43, 9611–9618.
663 <https://doi.org/10.1002/2016GL069949>

664

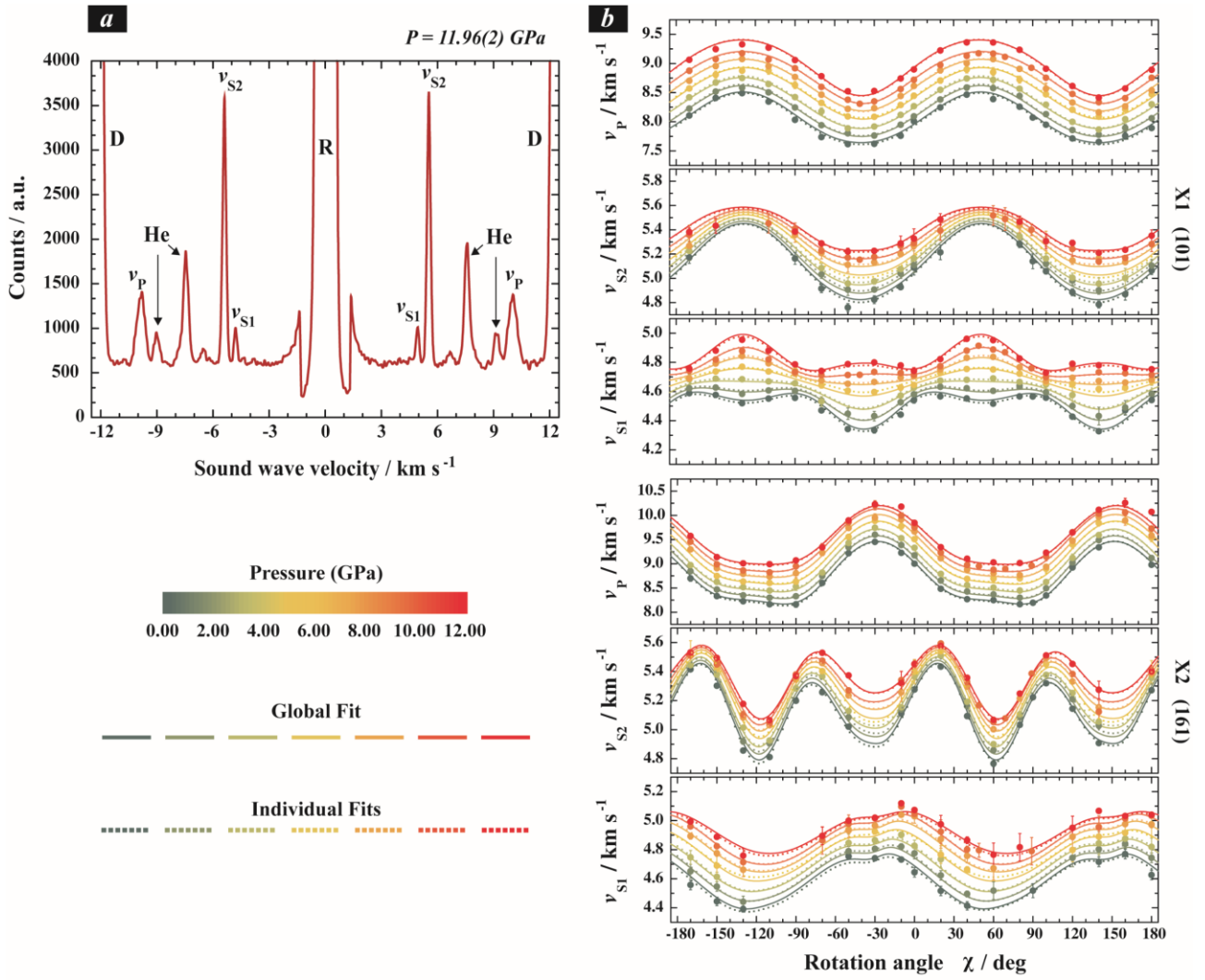


668 **Figure 1.** (a) Secondary electron image of a Fo90 olivine platelet oriented parallel to the (161) plane
669 (crystal X2) after the FIB cutting procedure; a superimposed yellow semicircle denotes the sample
670 that was then loaded in the DAC. (b) Cross-polarized light photomicrographs of platelet X2 (161)
671 and X1 (101) inside the sample chamber of the DAC at high pressure, together with a ruby chip (dark
672 black sphere on the left of 101 platelet).

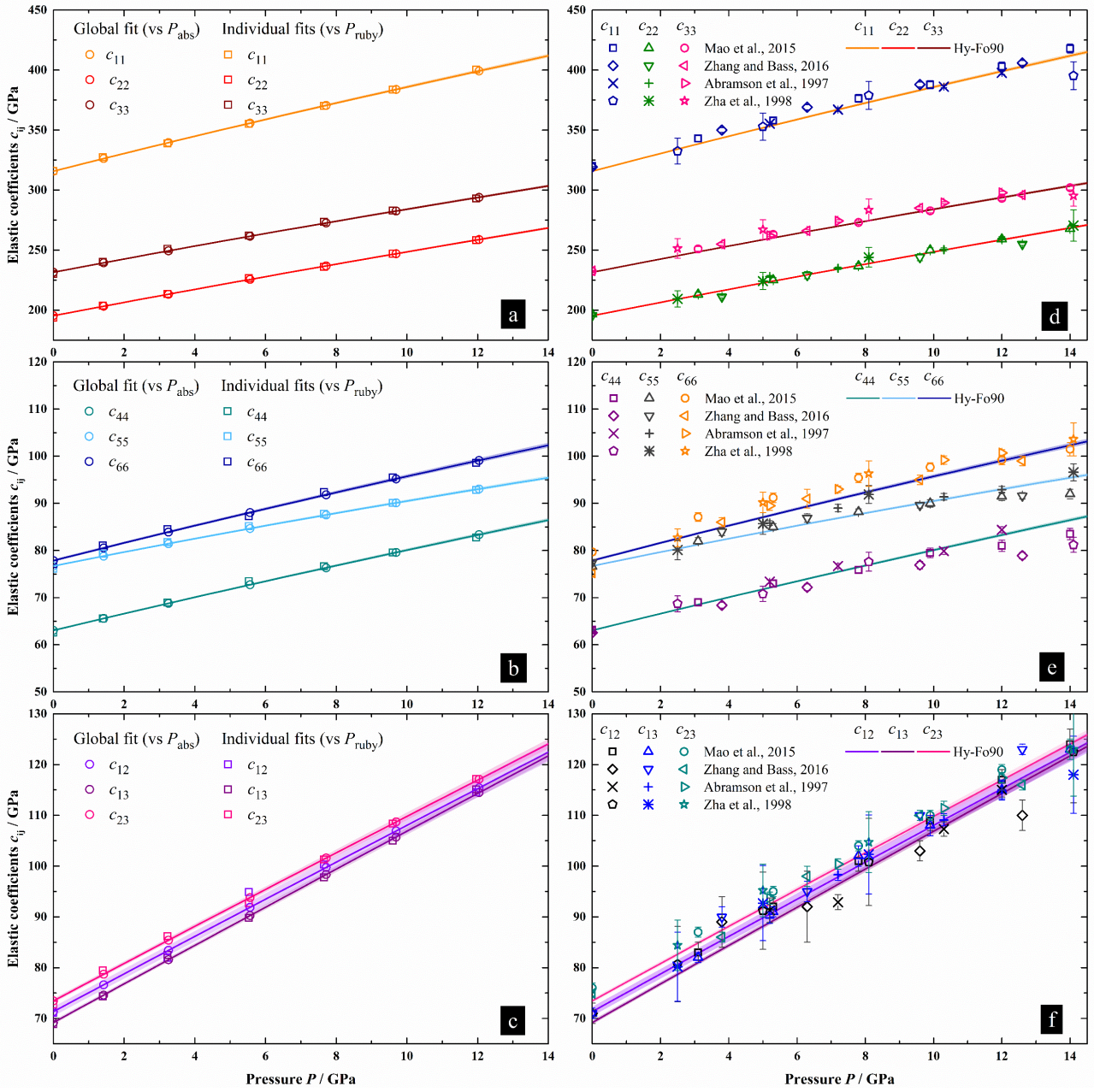


673

674 **Figure 2.** Unit-cell parameters and unit-cell volumes (inset) of crystals X1 and X2 normalized with
 675 respect to their room pressure values; data were fitted with a third-order Birch-Murnaghan EoS using
 676 the EosFit7c program (Angel et al., 2014). Literature data of anhydrous Fo90-92 olivines (Nestola et
 677 al., 2011; Zha et al., 1998; Supplementary Table S1) are shown for reference. Note the good
 678 agreement between the BM3 fits and relative compression data of hydrous Fo90 olivine and the
 679 literature data for the corresponding anhydrous phase.

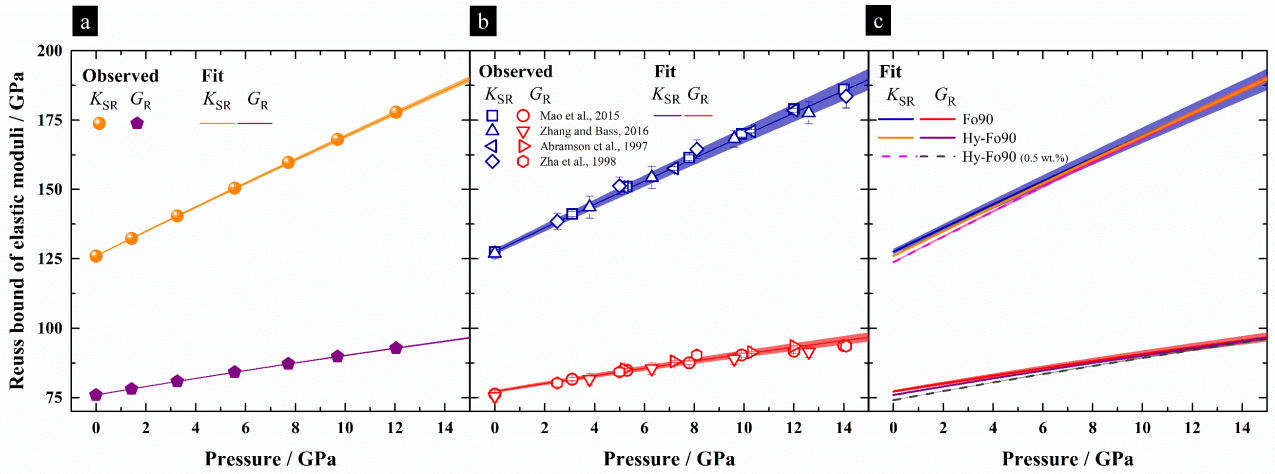


680
 681 **Figure 3.** (a) Selected Brillouin spectrum of crystal X2 (161) at 11.96(2) GPa showing distinct and
 682 well-resolved compressional v_P , slow and fast shear v_{S1} and v_{S2} wave velocities peaks, as well as
 683 spectral contributions of the diamond anvils (D), pressure medium (He) and elastic scattering (R). (b)
 684 Data points (filled symbols) as a function of the rotation angle (χ) for both platelets and dispersion
 685 curves obtained from the global fit (solid lines) and individual fits (dashed lines), showing excellent
 686 agreement between the two fitting strategies.



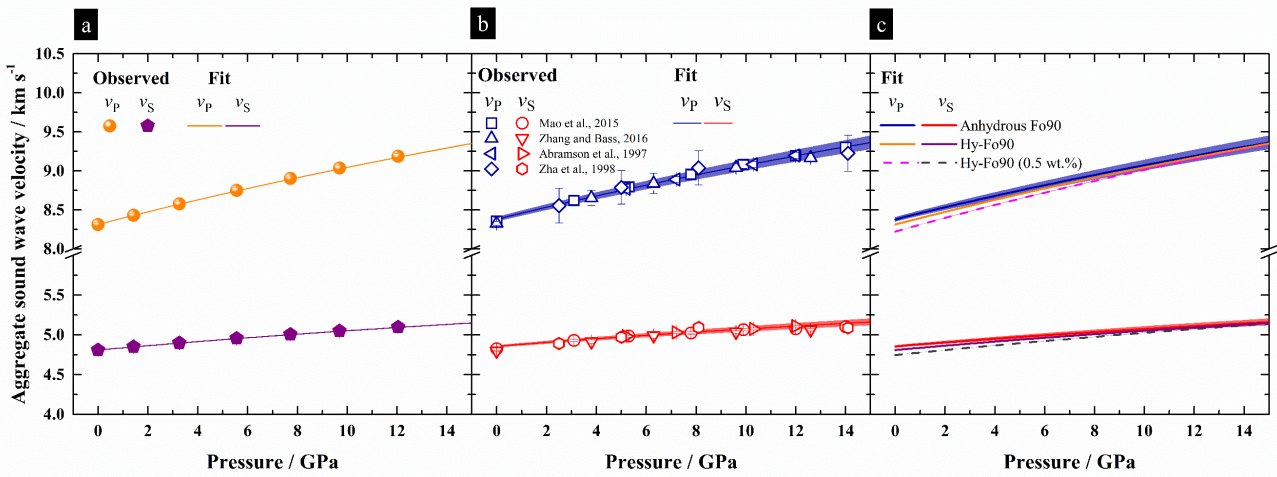
687

688 **Figure 4.** (a-b-c) Comparison of the c_{ij} obtained through the global fit (open circles) and individual
689 fits (open squares), showing values typically identical within two standard deviations (Table 2); the
690 solid lines represent 3rd order EoS fits of each c_{ij} (global fit parameters) (Table 3). (d-e-f) Comparison
691 of the c_{ij} of anhydrous Fo90 olivines selected from previous literature (Abramson et al., 1997; Mao
692 et al., 2015; Zha et al., 1998; Zhang and Bass, 2016; Supplementary Table S2), and the fits of each
693 c_{ij} (global fit parameters) of hydrous Fo90 olivine obtained in this study. Note that the fits of the
694 experimentally determined c_{ij} s for hydrous olivine and the c_{ij} s of the corresponding anhydrous phase
695 are nearly identical.



696

697 **Figure 5.** (a) Variation as a function of pressure of the bulk (K) and shear (G) moduli of hydrous
 698 Fo90 calculated in the Reuss bound from the experimental high-pressure elasticity measurements of
 699 this study; the solid line and shaded area are the fit of the experimental data and the associated
 700 uncertainty, respectively. (b) Variation as a function of pressure of the bulk (K) and shear (G) moduli
 701 of anhydrous Fo90 calculated in the Reuss bound from previous experimental high-pressure elasticity
 702 measurements (Abramson et al., 1997; Mao et al., 2015; Zha et al., 1998; Zhang and Bass, 2016;
 703 Supplementary Table S2); the solid line and shaded area are the fit of the experimental data and the
 704 associated uncertainty, respectively. (c) Superimposition of fit curves for hydrous Fo90 and
 705 anhydrous Fo90 olivine; the dashed lines represent a linear extrapolation of the effect of incorporation
 706 of 0.5 wt. % H₂O on the elastic properties of Fo90 olivine (see text and Table 4). Uncertainties are
 707 calculated by propagating the experimental errors on density and elastic moduli.



708

709 **Figure 6.** (a) Variation as a function of pressure of the aggregate compressional and shear wave
 710 velocities of hydrous Fo90 calculated from the experimental high-pressure elasticity measurements
 711 of this study; the solid line and shaded area the fit of the experimental data and the associated
 712 uncertainty, respectively. (b) Variation as a function of pressure of the aggregate compressional and
 713 shear wave velocities of anhydrous Fo90 calculated from previous experimental high-pressure
 714 elasticity measurements (Abramson et al., 1997; Mao et al., 2015; Zha et al., 1998; Zhang and Bass,
 715 2016; Supplementary Table S2); the solid line and shaded area the fit of the experimental data and
 716 the associated uncertainty, respectively. (c) Superimposition of fit curves for hydrous Fo90 and
 717 anhydrous Fo90 olivine. Uncertainties are calculated by propagating the experimental errors on
 718 density and elastic moduli.

719 **Tables**

720

721 **Table 1.** Unit-cell lattice parameters and volumes of hydrous Fo90 olivine crystals X1 and X2 measured in the DAC experiment. Pressure is calculated

722 using the ruby fluorescence calibration of Shen et al. (2020).

P (GPa)	X1 (platelet 1 0 1)				X2 (platelet 1 6 1)			
	a (Å)	b (Å)	c (Å)	V (Å³)	a (Å)	b (Å)	c (Å)	V (Å³)
0.00010(1)	4.7613(5)	10.2243(2)	5.9925(3)	291.72(3)	4.7610(1)	10.2227(3)	5.9921(1)	291.63(1)
1.40(2)	4.7499(7)	10.1753(3)	5.9701(5)	288.55(4)	4.7487(3)	10.1744(5)	5.9700(3)	288.44(2)
3.23(2)	4.7351(5)	10.1147(3)	5.9432(4)	284.64(3)	4.7342(2)	10.1128(4)	5.9423(2)	284.49(2)
5.53(4)	4.7178(7)	10.0455(3)	5.9116(5)	280.16(3)	4.7176(2)	10.0436(4)	5.9108(2)	280.06(2)
7.66(2)	4.7029(6)	9.9847(3)	5.8837(4)	276.28(3)	4.7028(3)	9.9824(7)	5.8826(3)	276.16(3)
9.60(4)	4.6902(7)	9.9313(3)	5.8592(6)	272.92(3)	4.6899(3)	9.9292(5)	5.8581(2)	272.80(2)
11.96(2)	4.6765(6)	9.8731(2)	5.8319(5)	269.27(3)	4.6762(2)	9.8707(4)	5.8309(1)	269.14(1)

723

724 **Table 2.** Elastic stiffness coefficients (c_{ij}) and elastic moduli obtained from the individual fit and global fit procedure, reported in GPa. Numbers in
725 brackets represent one standard deviation (std). ρ uncertainties propagate both the std's of the unit-cell volumes from SCXRD and the chemical
726 composition from EPMA.

Individual Fits

P (GPa)	ρ (g cm⁻³)	c_{11}	c_{22}	c_{33}	c_{44}	c_{55}	c_{66}	c_{12}	c_{13}	c_{23}	K_{SV}	G_V	K_{SR}	G_R	$K_{S\ VHR}$	G_{VHR}
0.00010(1)	3.345(6)	316.1(9)	193.7(6)	230.2(6)	62.6(2)	76.1(2)	77.1(3)	70.8(1.1)	68.8(5)	72.8(5)	129.4(4)	78.3(1)	125.2(4)	75.4(1)	127.3(4)	76.9(1)
1.40(2)	3.382(6)	327.3(6)	203.6(3)	240.2(5)	65.6(2)	79.3(2)	81.1(2)	74.3(1.0)	74.4(6)	79.5(4)	136.4(4)	81.4(1)	132.3(4)	78.4(1)	134.3(4)	79.9(1)
3.23(2)	3.428(6)	339.0(6)	213.4(4)	251.1(5)	69.0(3)	81.8(2)	84.5(3)	82.0(9)	82.5(4)	86.2(4)	145.0(3)	83.9(1)	140.7(3)	81.1(1)	142.8(3)	82.5(1)
5.53(4)	3.483(6)	355.1(1.1)	226.7(4)	262.1(6)	73.5(2)	85.2(5)	87.2(5)	94.9(1.8)	89.8(7)	92.7(7)	155.4(5)	87.0(1)	150.9(5)	84.4(1)	153.2(5)	85.7(1)
7.66(2)	3.532(6)	370.3(1.0)	236.0(4)	273.4(8)	76.7(2)	87.8(2)	92.4(3)	100.3(1.3)	97.8(6)	101.3(6)	164.3(4)	90.0(1)	159.6(4)	87.4(1)	162.9(4)	89.2(1)
9.60(4)	3.575(6)	383.9(1.0)	247.0(5)	282.9(7)	79.6(2)	90.1(3)	95.5(3)	108.3(1.5)	105.1(6)	108.4(7)	173.0(5)	92.5(1)	168.2(4)	89.8(1)	170.6(4)	91.2(1)
11.96(2)	3.624(6)	400.4(1.4)	258.4(8)	293.0(1.0)	82.8(3)	92.8(3)	98.6(4)	114.5(1.6)	115.2(8)	117.2(8)	182.8(5)	95.2(1)	177.7(5)	92.4(1)	180.3(5)	93.8(1)

Global Fit

0.00010(1)	3.345(6)	315.7(7)	193.3(4)	231.5(5)	63.0(2)	76.7(2)	77.8(3)	71.3(9)	69.2(4)	73.5(4)	130.1(3)	78.8(1)	126.0(2)	75.9(1)	128.0(3)	77.3(1)
1.424(7)	3.382(6)	326.3(7)	203.2(4)	239.4(5)	65.6(2)	78.8(2)	80.5(3)	76.6(9)	74.6(4)	78.7(4)	136.5(3)	80.9(1)	132.4(2)	78.1(1)	134.4(3)	79.5(1)
3.26(2)	3.428(6)	339.6(8)	213.2(4)	249.4(5)	68.8(2)	81.5(2)	83.9(3)	83.4(1.0)	81.6(4)	85.4(5)	144.8(3)	83.6(1)	140.4(3)	80.8(1)	142.6(3)	82.2(1)
5.56(3)	3.483(6)	355.8(9)	225.6(5)	261.5(6)	72.7(2)	84.7(2)	88.1(3)	91.9(1.1)	90.3(5)	93.8(5)	155.0(4)	86.9(1)	150.5(3)	84.2(1)	152.7(3)	85.5(1)
7.72(4)	3.532(6)	370.6(1.0)	236.8(6)	272.6(7)	76.3(3)	87.6(3)	91.8(4)	99.7(1.3)	98.3(6)	101.6(6)	164.4(4)	89.8(1)	159.7(3)	87.1(1)	162.0(4)	88.5(2)
9.69(5)	3.575(6)	383.9(1.2)	246.9(7)	282.5(9)	79.6(3)	90.1(3)	95.2(4)	106.9(1.5)	105.7(7)	108.7(7)	172.9(5)	92.4(1)	168.1(3)	89.8(1)	170.5(4)	91.1(2)
12.04(7)	3.624(6)	399.3(1.4)	258.8(8)	294.0(1.0)	83.4(3)	93.1(3)	99.1(5)	115.4(1.7)	114.5(8)	117.1(8)	182.9(5)	95.4(1)	177.9(4)	92.8(1)	180.4(5)	94.1(2)

728 **Table 3.** Resulting fit parameters of the third-order finite strain expression for the c_{ij} and c'_{ij} shown in Figure 4.

	c_{ij}	c'_{ij}
c_{11}	315.7(7)	7.21(9)
c_{22}	195.3(4)	5.41(5)
c_{33}	231.5(5)	5.41(6)
c_{44}	63.0(2)	1.74(2)
c_{55}	76.7(2)	1.46(2)
c_{66}	77.8(3)	1.84(3)
c_{12}	71.3(9)	3.59(11)
c_{13}	69.2(4)	3.68(5)
c_{23}	73.5(4)	3.56(5)

729

730 **Table 4.** EoS parameters for K and G in the Voigt and Reuss bound for hydrous and anhydrous Fo90 olivine.

Anhydrous Fo90 olivine – best fit

	K_{SV}	G_V	K_{SR}	G_R
M_0 (GPa)	131.8(1.0)	80.2(5)	127.5(1.0)	77.2(5)
M'_0	4.29(14)	1.42(5)	4.33(14)	1.48(6)

This study – Hydrous Fo90 olivine (global fit parameters)

	K_{SV}	Effect of H_2O (%)	G_V	Effect of H_2O (%)	K_{SR}	Effect of H_2O (%)	G_R	Effect of H_2O (%)
M_0 (GPa)	130.1(2)	-1.3	78.76(8)	-1.8	126.0(2)	-1.2	75.92(8)	-1.7
M'_0	4.41(4)	2.8	1.49(1)	4.9	4.46(4)	3.0	1.54(1)	4.1

Hydrous Fo90 olivine – extrapolation to 0.5 wt. % H_2O

	K_{SV}	Effect of H_2O (%)	G_V	Effect of H_2O (%)	K_{SR}	Effect of H_2O (%)	G_R	Effect of H_2O (%)
M_0 (GPa)	127.6(2)	-3.2	76.60(8)	-4.5	123.8(2)	-2.9	74.00(8)	-4.1
M'_0	4.59(4)	7.0	1.60(1)	12.3	4.66(4)	7.5	1.63(1)	10.1

$\Delta_{H_2O}M$ (%/wt. % H_2O) – Hydrous Fo90 olivine

	K_{SV}	G_V	K_{SR}	G_R
M_0 (GPa)	-6.4(4.0)	-9.0(3.4)	-5.9(4.1)	-8.3(3.5)
M'_0	14.0(17.5)	24.7(19.2)	15.0(17.4)	20.3(21.6)

$\Delta_{H_2O}M$ (%/wt. % H_2O) – Hydrous Fo100 olivine [data from Mao et al., 2010 and Zha et al., 1996]

	K_{SV}	G_V	K_{SR}	G_R
M_0 (GPa)	-3.1(0.9)	-3.2(0.7)	-2.2(0.9)	-3.2(0.7)
M'_0 ¹	7.9(5.9)	27.8(11.1)	7.9(5.9)	27.8(11.1)

731

¹ We assumed that M'_0 in the Voigt-Reuss-Hill bound $\approx M'_0$ in the Voigt and Reuss bounds